IEEE Open Journal of
Antennas and Propagation

Received 3 August 2021; revised 30 August 2021; accepted 7 September 2021. Date of publication 13 September 2021;
date of current version 21 September 2021.

Digital Object Identifier 10.1109/OJAP.2021.3111834

Theoretical Analysis of Beam-Steerable, Broadside-Radiating Huygens Dipole Antenna Arrays and Experimental Verification of an Ultrathin Prototype for Wirelessly Powered IoT Applications

WEI LIN (Senior Member, IEEE), AND RICHARD W. ZIOLKOWSKI (Life Fellow, IEEE)

Global Big Data Technologies Centre, School of Electrical and Data Engineering, Faculty of Engineering and IT,
University of Technology Sydney, Ultimo, NSW 2007, Australia

CORRESPONDING AUTHOR: W. LIN (e-mail: wei.lin@uts.edu.au)

This work was supported in part by the Australia Research Council Discovery Early Career Researcher Award under Grant PRO20-9959,
and in part by the UTS Chancellor's Postdoctoral Fellowship under Grant PRO18-6147.

ABSTRACT The theoretical analysis of beam-steerable, broadside-radiating Huygens dipole antenna arrays (HDAAs) is presented. Linear HDAAs with different numbers of elements are investigated and compared with full-wave simulations. Their attractive performance characteristics for wirelessly powered IoT applications are emphasized. Each Huygens dipole antenna (HDA) is an electrically small, linearly polarized, efficient, unidirectional radiating element. Linear HDAAs are confirmed to achieve high directivity beams in one principle plane and significantly broad beamwidths in the orthogonal principle plane. Very stable gain variation when their main beam is steered is demonstrated. A practical beam-steerable, broadside-radiating, linear HDAA is developed that employs an experimentally-verified HDA and is facilitated by a microstrip power-divider feed network. The entire HDAA design is ultrathin ($\lambda_0/240.87$), lying only on a single piece Rogers Duroid^{TM} 5880 copper-clad substrate. A proof-of-concept 3-element HDAA prototype excited with a 3×3 Butler matrix centered at 2.45 GHz was designed, fabricated and measured. The measured results, in very good agreement with their simulated values, demonstrate the efficacy of the linear HDAA designs and their potential usefulness for wireless power transfer (WPT) systems dedicated to emerging IoT applications that require power be directed towards terminals in multiple specified directions with broad area coverage at each one.

INDEX TERMS Antenna arrays, beam-steering, Butler matrix, electrically small antennas, Huygens dipole antennas, wireless power transfer (WPT).

I. INTRODUCTION

ANTENNA characteristics such as high directivity and wide beamwidth are highly desired in wireless applications that require long distance operation and multi-user coverage [1]–[3]. For example, base station antennas that are used for emerging wireless power transfer (WPT) applications should have both high gain and large half-power beamwidth (HPBW) performance characteristics in order to broadcast and deliver wireless power to a large number of widely distributed Internet-of-Things (IoT) sensors [4]. However, it has been challenging and even believed to be contradictory to achieve both features simultaneously in compact and low-cost antenna designs. One practical approach to this issue is to design a high directivity linear antenna array with a narrow beamwidth in one principal plane and with wide beamwidth in the orthogonal plane [5]–[10], and then to insist that the array be capable of steering its narrow beam in order to enlarge its coverage.

Fig. 1 illustrates one practical application example of the aforementioned antenna array for broadcasting wireless power to multiple remotely-located IoT devices, e.g., rectenna-enabled sensors used in a smart agricultural ecosystem. Wide horizontal coverage of multiple sensor arrays sparsely distributed at different elevations would be desired. It is clearly seen that such an application requires a power transmitting array that features high gain, wide horizontal patterns and elevation beam-steering.

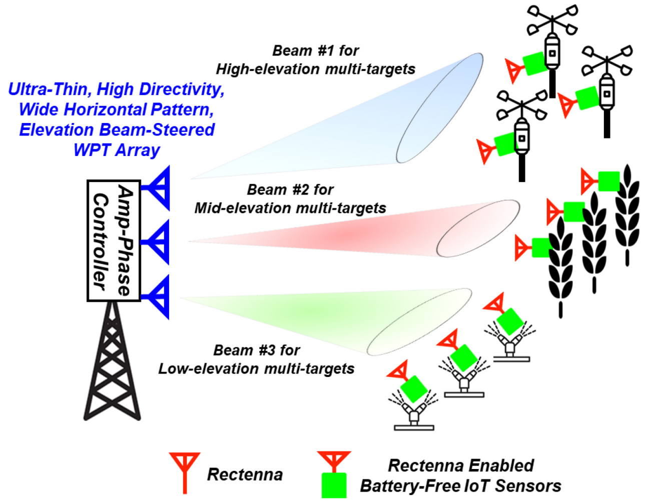

FIGURE 1. *Application example:* Vertical-oriented linear HDAA broadcasting wireless power to multiple battery-free IoT targets in a smart agriculture ecosystem at different elevations with wide horizontal coverage, e.g., to anemometers on tall masts that sense the wind speed, to temperature and humidity sensors embedded in crops, and to moisture sensors at ground level near water sprinklers.

Linear antenna arrays with beam-steering or multi-beam performance have been extensively studied, e.g., [11]–[24]. One very popular design methodology is to adopt a Butler matrix as the beamforming feed network that excites a linear array of antenna elements. Element choices have included horn antennas [11], varieties of slot antennas [12]–[17], microstrip patch antennas [18]–[20], modified dipoles [21]–[24] and magnetoelectric (ME) dipole antennas [25]. A challenge all of these designs share is being able to simultaneously achieve a wide (3-dB) HPBW, e.g., larger than 150° in the principal vertical plane that is orthogonal to the array axis; high radiation efficiency; compact size; and easy, cost-effective implementation on a single piece of PCB substrate.

For instance, the four microstrip-line-fed double-ridge gap waveguide (DRGW) horn antennas in [11] were arranged linearly and were excited by a 4×4 Butler maxtrix. Its HPBW in that vertical, orthogonal plane was only 117°. Moreover, the required metallic fabrication costs are notably expensive. Other reported examples that use quasi-unidirectional array elements in a linear arrangement include beam-steerable slot antenna arrays enabled by longitudinal slot radiators [12]–[15], tapered slot antennas (TSAs) [16], and CP slot elements [17]. All of these slot-based designs again have narrow beamwidths in that vertical, orthogonal plane, i.e., the largest achieved HPBW is less than 120° [17]. Multi-beam linear microstrip patch antenna arrays have also been developed [18]–[20]. Their beamwidths in that vertical orthogonal plane are again narrow, being restricted by the beamwidth of each patch antenna element. Both the slot and patch arrays achieve their quasi-unidirectional performance by the presence of a large ground plane under all of their elements. While the corresponding linear dipole arrays [21]–[24] are able to achieve very wide beamwidths, they radiate bidirectionally or require a large ground plane. For example, the linear V-shaped dipole array reported in [24] achieved a HPBW larger than 150°. However, the radiation pattern has a dip in the broadside direction due to the V-shaped dipole structure. As a consequence, the peak realized gain decreases and the cross polarization level is high. On the other hand, a linear ME dipole antenna array was developed in [25] that achieves a HPBW larger than 150°. Nonetheless, the design requires multiple PCB layers and its implementation is not easy.

We report in this paper the first comprehensive theoretical analysis of beam-steerable, broadside-radiating Huygens dipole antenna arrays (HDAAs). Moreover, we report the first design and realization an ultrathin HDAA prototype based on a linear arrangement of electrically small, Huygens dipole antennas (HDAs) along with measured results that confirm its simulated performance characteristics, confirming the efficacy of the HDAA concepts. The theoretical analysis demonstrates the beam-steering performance characteristics with different numbers of HDAs. The theoretical results and the consequent advantages of HDAAs are highlighted and confirmed with detailed, realistic simulations. Excellent radiation performance is achieved that successfully addresses the aforementioned challenges to achieve a high directivity beam that is steerable in one principle plane and has a significantly wide (3-dB) HPBW in the orthogonal principle plane. The HDAAs exhibit attractive features including a large front-to-back-ratio (FTBR), beam-steering with small gain variation, and high radiation efficiency. Moreover, the reported realizable linear HDAAs have the practical advantages of being ultrathin, compact, easy to fabricate and low cost. An optimized proof-of-concept linear HDAA prototype integrated with a Butler matrix feed network was fabricated and tested successfully, confirming the analysis and simulation results. The developed linear HDAAs are ideal candidates for various wireless applications, notably WPT-based ecosystems that require power be directed towards IoT devices in multiple specified directions with broad area coverage at each one, e.g., as the base station WPT antenna system for powering a large number of remotely distributed battery-free IoT devices [26].

The remaining sections of this paper are organized as follows. The theoretical analysis is developed first in Section II, supplemented with additional details in the Appendix. An HDA excited by an ideal differential source and HDAAs formed with it are introduced in Section III. The HDA is a version of the innovative ultrathin electrically small HDA reported in [27] as a WPT receiver at 915 MHz. It is modified herein to act as a transmitting element excited by an ideal differential source at 2.45 GHz. The practical design and implementation of HDAAs formed with this HDA are then presented in Section IV. The measured results of an optimized proof-of-concept prototype verify the efficacy of the HDAA concept. Section V draws some conclusions.

All of the numerical simulations and their optimized configurations reported herein were performed using the commercial software packages: MATLAB and ANSYS Electromagnetics Suite (HFSS), v. 18. The simulation models employed the known, real properties of the associated dielectrics and conductors.

II. THEORETICAL ANALYSIS OF BEAM-STEERABLE HUYGENS DIPOLE ANTENNA ARRAYS

A brief review of the analysis and physics of a Huygens dipole source is given, emphasizing its cardioid radiation performance characteristics. The general analysis of an array of Huygens dipole sources is then developed. Comparisons with comparable arrays of electric dipole antennas are given to elucidate the performance advantages that HDAAs offer.

A. HUYGENS DIPOLE SOURCE

As derived in the Appendix, the electric fields generated by a balanced pair of an infinitesimal electric current (J) moment $I_e = I_0\ell\,\hat{y}$ and a magnetic current (K) moment $I_m = -\eta I_0\ell\,\hat{x}$ in the far field are:

$$\vec{E}^{ff}_{\omega,J}(\vec{r}) = j\,\omega\mu\,I_0\ell\frac{e^{-jkr}}{4\,\pi\,r}\left(\hat{r}\times\hat{r}\times\hat{y}\right)$$
$$\vec{E}^{ff}_{\omega,K}(\vec{r}) = -j\,\omega\mu\,I_0\ell\frac{e^{-jkr}}{4\,\pi\,r}\left(\hat{r}\times\hat{x}\right) \tag{1}$$

Therefore, the total far field for an infinitesimal electric and magnetic dipole pair is

$$\vec{E}^{ff}_{\omega,\text{total}}(\vec{r}) = j\,\omega\mu\,I_0\ell\frac{e^{-jkr}}{4\,\pi\,r}\vec{\mathcal{P}}(\theta,\phi)$$
$$\vec{H}^{ff}_{\omega,\text{total}}(\vec{r}) = \frac{1}{\eta}\hat{r}\times\vec{E}^{ff}_{\omega,\text{total}}(\vec{r}) \tag{2}$$

where the angular variation of the vector field calculated with the vector product expressions given in the Appendix is:

$$\begin{aligned}\vec{\mathcal{P}}(\theta,\phi) &= \left[\left(\hat{r}\times\hat{r}\times\hat{y}-\hat{r}\times\hat{x}\right)\right] = \sin^2\theta\sin\phi\cos\phi\hat{x}\\ &\quad-\left(\cos^2\theta+\sin^2\theta\cos^2\phi+\cos\theta\right)\hat{y}\\ &\quad+\left[\sin\theta\sin\phi+\sin\theta\cos\theta\sin\phi\right]\hat{z}\end{aligned} \tag{3}$$

In the yz-plane with $\phi = \pi/2$ one then has

$$\vec{\mathcal{P}}(\theta,\phi=\pi/2) = -(1+\cos\theta)\left[\cos\theta\hat{y}-\sin\theta\hat{z}\right] \tag{4}$$

Similarly, in the zx-plane with $\phi = 0$ one also has

$$\vec{\mathcal{P}}(\theta,\phi=0) = -(1+\cos\theta)\hat{y} \tag{5}$$

The cardioid factor: $(1+\cos\theta)$, characteristic of a Huygens source field, is recognized immediately, i.e., the total fields are null along the negative z-axis, where $\theta = \pi$, and are increased by a factor of 2 along the +z-axis.

The corresponding time-averaged Poynting's vector and the total power radiated are given by the expressions

$$\begin{aligned}\vec{S}_{\text{total}}(\vec{r}) &= \frac{1}{2}\text{Re}\left\{\vec{E}^{ff}_{\omega,\text{total}}(\vec{r})\times\left[\vec{H}^{ff}_{\omega,\text{total}}(\vec{r})\right]^*\right\}\\ &= \frac{1}{2\eta}\left|\vec{E}^{ff}_{\omega}(\vec{r})\right|^2\end{aligned} \tag{6}$$

$$P^{rad}_{\text{total}} = \oiint_{S^2_\infty} d\Omega\;\hat{r}\cdot\vec{S}_{\text{total}}(\vec{r}) \tag{7}$$

where S^2_∞ is the sphere (S^2) centered on the origin and whose radius is infinitely large. The directivity follows as

$$D(\theta,\phi) = \frac{4\pi r^2\vec{S}_{\text{total}}(\vec{r})\cdot\hat{r}}{P^{rad}_{\text{total}}} \tag{8}$$

Consequently, the balanced electric and magnetic dipole pair gives

$$\vec{S}(\vec{r}) = \frac{1}{2}(k\ell)^2\eta|I_0|^2\frac{1}{(4\pi r)^2}(1+\cos\theta)^2\hat{r} \tag{9}$$
$$P^{rad}_{tot} = \frac{(k\ell)^2}{6\pi}\eta\,|I|^2 = 2\times\left[\frac{\pi}{3}\left(\frac{\ell}{\lambda}\right)^2\eta\,|I|^2\right] \tag{10}$$

Thus, the total power radiated is twice the total power radiated by either dipole individually. The directivity follows as

$$D(\theta,\phi) = \frac{4\pi r^2\vec{S}(\vec{r})\cdot\hat{r}}{P^{rad}_{tot}} = \frac{3}{4}(1+\cos\theta)^2 \tag{11}$$

Therefore, the maximum directivity of the electric-magnetic dipole pair ($\mathcal{N} = 1$), which is along the positive z-axis, is 3, twice the value of either dipole alone confirming the Harrington result [28], [29]: $D_{max} = \mathcal{N}^2 + 2\times\mathcal{N} = 1^2 + 2\times 1 = 3$.

A MATLAB program was created to compute the performance characteristics of an infinitesimal electric dipole oriented along the y-axis and the basic Huygens dipole pair with its electric and magnetic dipoles oriented, respectively, along the +y and −x axes. The integrals of the total radiated power (7) were calculated numerically. The directivity of the electric and Huygens dipole antennas obtained in this manner are shown in Fig. 2. The figure-eight pattern of the dipole element in the principle vertical plane containing the dipole (E-plane) and the omnidirectional pattern in the principal vertical plane orthogonal to it and the cardioid pattern of the Huygens element in both principal planes are clearly identified. The peak directivity of the electric dipole antenna and the HDA are 1.76 and 4.77 dB, respectively. The algorithms to attain these results were integrated into the array calculations considered next as test cases for them. Thus, as will be illustrated below, a linear HDAA has two immediate advantages over a linear array of electric dipole antennas, i.e., it yields unidirectional rather than bidirectional patterns and has a factor of 3 dB (2 times) larger peak directivity.

B. ARRAY OF HUYGENS DIPOLE SOURCES

The corresponding results for a finite number of electric and magnetic current sources in three dimensions follows by superposition. In particular, consider a set of N electric and magnetic elemental current sources located at the points $\vec{r}_n = x_n\,\hat{x} + y_n\,\hat{y} + z_n\,\hat{z}$, $n = 1,\ldots,N$, in $\mathbb{R}^3$:

$$\vec{J}_n(\vec{r}) = I_{e,n}\ell_{e,n}\delta(x-x_n)\,\delta(y-y_n)\,\delta(z-z_n)\hat{u}_n$$
$$\vec{K}_n(\vec{r}) = I_{m,n}\ell_{m,n}\delta(x-x_n)\,\delta(y-y_n)\,\delta(z-z_n)\hat{v}_n \tag{12}$$

The electromagnetic fields in the far field of these sources referenced to the coordinate origin follow immediately from

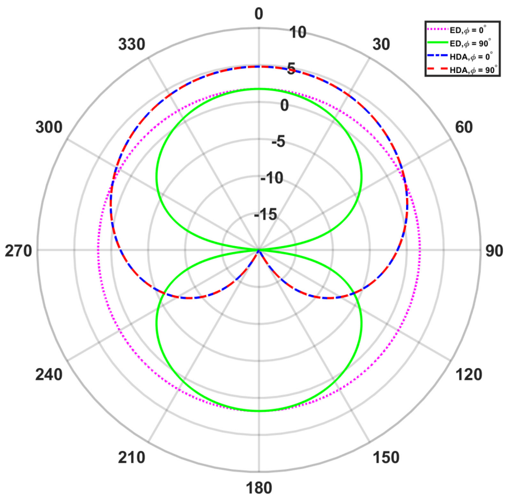

FIGURE 2. **The directivity pattern in the yz-plane for the electric dipole and the Huygens dipole antennas. $\theta = 0°$ is the broadside direction.**

the Appendix results (27) and (28):

$$\vec{E}^{ff}_{\omega,J_n}(\vec{r}) = +j\,\omega\,\mu I_{e,n}\ell_{e,n}\frac{e^{-jkr}}{4\,\pi\,r}e^{+j\,k\hat{r}\cdot\vec{r}_n}\left(\hat{r}\times\hat{r}\times\hat{u}_n\right)$$
$$\vec{H}^{ff}_{\omega,K_n}(\vec{r}) = +j\,\omega\,\varepsilon I_{m,n}\ell_{m,n}\frac{e^{-jkr}}{4\,\pi\,r}e^{+j\,k\hat{r}\cdot\vec{r}_n}\left(\hat{r}\times\hat{r}\times\hat{v}_n\right) \quad (13)$$

Consequently, with balanced current moments: $I_{m,n}\ell_{m,n} = \eta I_{e,n}\ell_{e,n} = \eta I_n\ell$ and with Eq. (25), the electric fields radiated into the far field by each of the electric and magnetic current sources of an N-element linear Huygens array are:

$$\vec{E}^{ff}_{\omega,J_n}(\vec{r}) = +j\,\omega\,\mu I_n\ell\frac{e^{-jkr}}{4\,\pi\,r}e^{+j\,k\hat{r}\cdot\vec{r}_n}\left(\hat{r}\times\hat{r}\times\hat{u}_n\right)$$
$$\vec{E}^{ff}_{\omega,K_n}(\vec{r}) = +j\,\omega\,\mu I_n\ell\frac{e^{-jkr}}{4\,\pi\,r}e^{+j\,k\hat{r}\cdot\vec{r}_n}\left(\hat{r}\times\hat{v}_n\right) \quad (14)$$

giving the total electric field

$$\vec{E}^{ff}_{\omega,\text{total}}(\vec{r}) = +j\,\omega\,\mu\,\ell\frac{e^{-jkr}}{4\,\pi\,r}\left\{\sum_{1}^{N}\left[I_n e^{+j\,k\hat{r}\cdot\vec{r}_n}\right]\times\left[\left(\hat{r}\times\hat{r}\times\hat{u}_n\right)+\left(\hat{r}\times\hat{v}_n\right)\right]\right\} \quad (15)$$

Clearly, the standard array factor and element factors can be identified. The total electric field radiated by the N-element Huygens array into the far field becomes:

$$\vec{E}^{ff}_{\omega,\text{total}}(\vec{r}) = +j\,\omega\,\mu\,\ell\frac{e^{-jkr}}{4\,\pi\,r}\times\sum_{n=1}^{N}\text{AF}_{n,\text{total}}(\theta,\phi)\overrightarrow{\text{EVF}}_{n,\text{total}}(\theta,\phi) \quad (16)$$

where the array factor and element vector factor are, respectively,

$$\text{AF}_{n,\text{total}}(\theta,\phi) = I_n e^{+j\,k\hat{r}\cdot\vec{r}_n}$$
$$\overrightarrow{\text{EVF}}_{n,\text{total}}(\theta,\phi) = \hat{r}\times\hat{r}\times\hat{u}_n + \hat{r}\times\hat{v}_n \quad (17)$$

Since all of the electric and magnetic dipoles of each Huygens pair are taken to be oriented the same, i.e., the electric dipoles are oriented as $+\hat{y}$ and the magnetic dipoles are oriented as $-\hat{x}$, the element vector factor is the same for all elements and the more standard array far-field expression is attained from (16):

$$\vec{E}^{ff}_{\omega,\text{total}}(\vec{r}) = +j\,\omega\,\mu\,\ell\frac{e^{-jkr}}{4\,\pi\,r}\times\text{AF}_{\text{total}}(\theta,\phi)\times\overrightarrow{\text{EVF}}(\theta,\phi) \quad (18)$$

where the terms:

$$\text{AF}_{\text{total}}(\theta,\phi) = \sum_{n=1}^{N} I_n e^{+j\,k\hat{r}\cdot\vec{r}_n}$$
$$\overrightarrow{\text{EVF}}(\theta,\phi) = \hat{r}\times\hat{r}\times\hat{y} - \hat{r}\times\hat{x} = \vec{\mathcal{P}}(\theta,\phi) \quad (19)$$

Several idealized HDAA results are now immediately accessible. We assume for simplicity and ease of notation that each array has an odd number of elements. It is assumed that all of the magnitudes of the sources are the same, i.e., $|I_n| = I_0$, and that the Huygens elements are displaced uniformly along the y-axis with the center-to-center distance being d. The element vector factor is known from the single element analysis. We take with no loss of generality the standard element separation distance $d = \lambda/2$.

The patterns in the E-plane (yz-plane with $\phi = \pi/2$) and the H-plane (zx-plane with $\phi = 0$) are presented. The steerable beam direction is specified in the E-plane by the angle $(\theta,\phi) = (\theta_0,\phi_0 = \pi/2)$. Thus, we have $k\hat{r}\cdot\vec{r}_n = nkd\sin\theta\sin\phi - \sin\theta_0$. To achieve a tilted beam in the yz-plane pointing in the θ_0 direction, a constant phase factor is introduced with the source amplitudes. The amplitudes relative to the center of the array take the form: $I_n = I_0\exp\{j[n-(N-1)/2]\,kd\sin\theta_0\sin\phi_0\}$ for $n = 1, 2, \ldots, N$ with, as noted, $\phi_0 = \pi/2$. Thus, the array factor takes on the conventional form

$$\text{AF}_{\text{total}}(\theta,\phi) = I_0\sum_{n=1}^{N} e^{+j\,[n-(N-1)/2]kd\,(\sin\theta-\sin\theta_0)} \quad (20)$$

The calculated directivity patterns in both principal planes for the single, three, and nine HDA element arrays that generate broadside beams pointing in the direction ($\theta = 0°, \phi = 90°$) are shown in Fig. 3. The maximum directivity for the one, three and nine element arrays is 4.77 dB (3), 9.17 dB (8.26) and 13.83 dB (24.15). We note that the approximate maximum directivity as obtained with [30](6-44) for a broadside-radiating array of nine isotropic elements is only $D_{max} \approx 2N(d/\lambda) = 9 = 9.54$ dB.

Similarly the calculated directivity results for the single, three, and nine HDA element arrays that generate beams pointing in the direction ($\theta = 30°, \phi = 90°$) are shown in Fig. 4. Their peak directivity values are 4.77 dB (3), 8.94 dB (7.84) and 13.61 dB (22.96). Note the narrowing of the HPBW of the beams in the E-plane and the maintenance

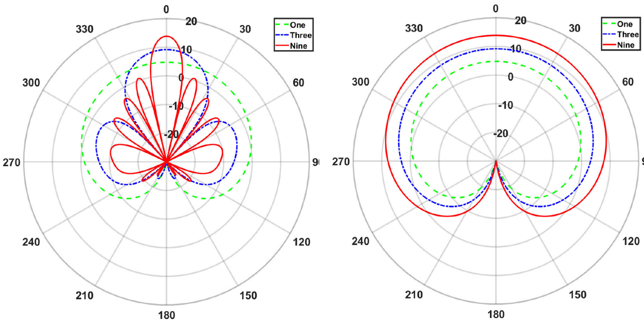

(a) $\phi = 90°$ (b) $\phi = 0°$

FIGURE 3. Directivity patterns in the two principal vertical planes for the one, three and nine element Huygens dipole antenna array radiating in the broadside direction.

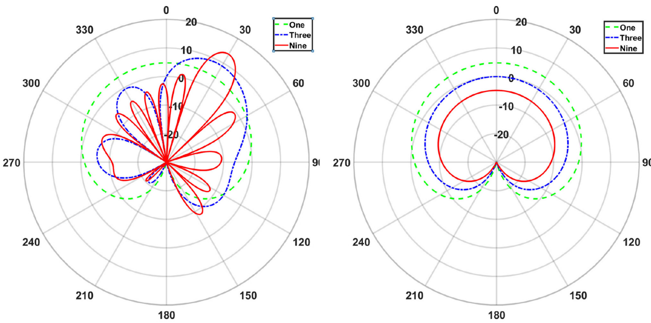

(a) $\phi = 90°$ (b) $\phi = 0°$

FIGURE 4. Directivity patterns in the two principal vertical planes for the one, three and nine element Huygens dipole antenna array radiating a directive beam pointed at ($\theta = 30°$, $\phi = 90°$) from in the broadside direction.

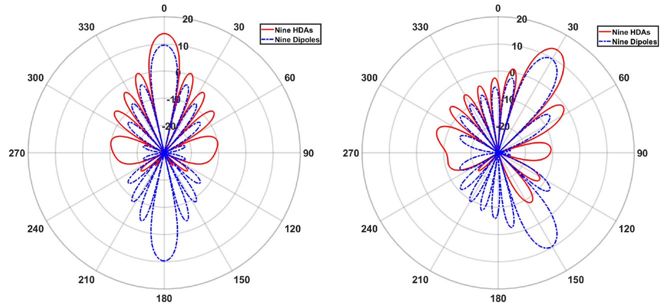

(a) $\theta_0 = 0°$ (b) $\theta_0 = 30°$

FIGURE 5. Directivity patterns in the principal vertical plane $\phi = 90°$ for the nine element HDA and electric dipole arrays. (a) Beam pointed in the broadside direction. (b) Beam pointed away from broadside.

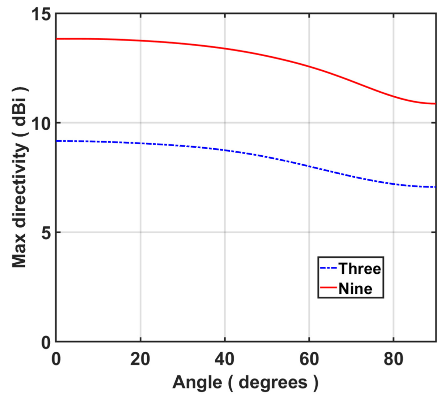

FIGURE 6. The maximum directivity in the yz-plane of the three and nine element HDAAs as functions of the beam angle θ_0.

of the very wide HPBW in the H-plane in both the broadside and beam-tilted cases as the number of array elements increases.

Comparisons of the nine element HDAA and the corresponding nine element electric dipole array for broadside ($\theta_0 = 0°$) and $\theta_0 = 30°$ directed beams are shown in Figs. 5(a) and 5(b), respectively. It is clear then that the Huygens dipole array yields slightly more than a 3 dB increase in the directivity over the array of electric dipole elements. The peak directivity of the HDA and dipole arrays is, respectively, 13.83 dBi and 9.66 dB in the broadside case and 13.61 and 9.66 dBi in the 30° case. The huge difference between them can be seen in the back direction where the dipole radiates with a FTBR = 0 dB versus FTBR $\sim \infty$ for the HDA array.

While its array factor is exactly pointed at $\theta_0 = 30°$, the maximum directivity of the HDAA differs very slightly from that direction simply because of the Huygens element pattern. The calculated maximum directivity of the three and nine element HDA arrays as the beam angle θ_0 is scanned from 0° to 90° is presented in Fig. 6. The directivity when $\theta_0 = 90°$ is 7.07 and 10.87 dB, for the three and nine element HDAA, respectively. The difference from the peak directivity in each case: 9.17 and 13.83 dB, is 2.10 and 3.56 dB, respectively. Thus, because of the very wide HPBW of an HDA, the 3-dB rolloff point of the HDAAs is pushed far towards the horizon. This is another interesting practical aspect of the HDAAs.

III. HDA EXCITED BY AN IDEAL DIFFERENTIAL SOURCE AND LINEAR HDAAS FORMED WITH IT

The proper selection of the single-element HDA is essential to achieve a high performance beam-steering array design. Among the many previously reported single-element HDA designs, e.g., the electrically small HDAs developed in [27], [31]–[33] and the related half-wavelength sized complementary magnetoelectric (ME) dipole antennas [34]–[38], the HDA in [27] was selected as the ideal candidate. In particular, it is an exceptionally thin, single-substrate electrically small HDA that was developed as a receiving element for WPT applications which do not require a wide bandwidth.

A. SINGLE HDA EXCITED BY AN IDEAL DIFFERENTIAL SOURCE

Its simulation model is shown in Fig. 7. The entire system is designed on a single piece of Rogers Duroid 5880 copper-clad substrate whose relative permittivity, loss tangent and thickness are 2.2, 0.0009 and 0.508 mm, respectively. This HDA consists of two electrically small metamaterial-inspired near-field resonant parasitic (NFRP) elements, an Egyptian

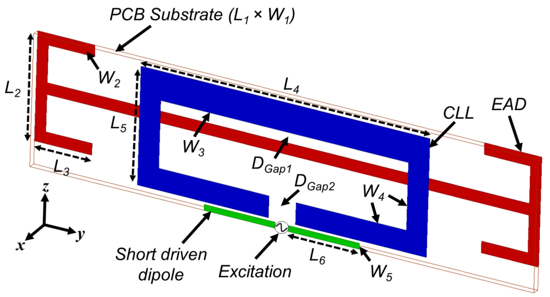

FIGURE 7. Optimized design of the ultrathin electrically small Huygens dipole antenna excited by an ideal differential source.

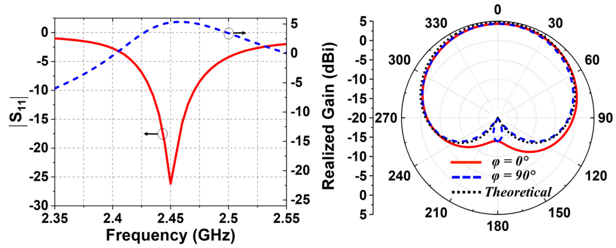

FIGURE 8. Simulated performance of the HDA design. (a) $|S_{11}|$ and realized gain values as functions of the source frequency. (b) Simulated and theoretical realized gain patterns at 2.45 GHz in the two principal vertical planes.

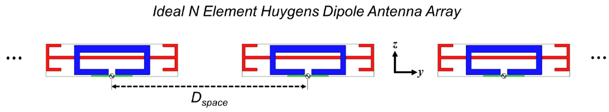

FIGURE 9. Configuration of the linear HDAA excited by ideal differential sources.

axe dipole (EAD) which acts as the electric dipole element and a capacitively-loaded loop (CLL) which acts as the magnetic dipole element. They are etched on opposite sides of the substrate. A short driven dipole is located on the same side as the CLL element and oriented along the y-axis. Its operating mechanisms are detailed in [27]. The original 915 MHz receiving design was integrated directly with a rectifier; it was modified herein to operate as a transmitter at 2.45 GHz. The optimized parameters of this ultrathin design at 2.45 GHz, i.e., 0.508 mm = $\lambda_0/240.97$, in terms of millimeters are: $L_1 = 37.0$, $L_2 = 7.6$, $L_3 = 4.2$, $L_4 = 21.2$, $L_5 = 8.2$, $L_6 = 5.2$, $W_1 = 9.2$, $W_2 = 0.8$, $W_3 = 2.0$, $W_4 = 1.5$, $W_5 = 0.4$, $D_{Gap1} = 1.0$, and $D_{Gap2} = 2.0$.

The simulated $|S_{11}|$ and realized gain values of the HDA as functions of the source frequency are shown in Fig. 8(a). The HDA is resonating at the target frequency, 2.45 GHz ($\lambda_0 = 122.36$ mm), in the 2.4–2.5 GHz ISM and WLAN bands. It is electrically small with $ka = 0.97 < 1$. The cardioid-shaped gain patterns radiated by the ideal (theoretically calculated in the Appendix) and realistic (simulated) HDAs at 2.45 GHz are shown in Fig. 8(b). The simulated results clearly agree quite well with the theoretical ones. The simulated (theory calculated) peak realized gain and FTBR values are 4.2 dBi (4.77 dBi) along the +z-direction and 18.2 (∞) dB, respectively. Analogous to the theoretical results, the simulated Huygens patterns are almost identical for both vertical planes, e.g., the E-plane with $\phi = 90°$ and the H-plane with $\phi = 0°$. The simulated HPBWs for the E- and H-planes are 130° (± 65°) and 138° (−64° to 74°), respectively. They are very close to the theoretical value, 132° (± 66°). The slight asymmetry in the simulated H-plane is due to the fact that the EAD and CLL radiators do not lie on the same surface; and, hence, it is associated with the thickness of the 5880 substrate.

B. HDAA DESIGN AND BEAM-STEERING PERFORMANCE

The unidirectional cardioid pattern radiated by the ultrathin HDA, its consequent 3 dB enhanced directivity over a simple dipole antenna, its very wide HPBW, and its ultrathin and compact size make it a very attractive element for a linear array. The developed uniform HDAA arrangement is illustrated in Fig. 9. The center-to-center distance between each of the elements is D_{space}. As anticipated from the theoretical analysis, high directivity beams with small variations in its peak realized gain value as the beam is steered in the E-plane ($\phi = 90°$) and a broad beamwidth in the H-plane ($\phi = 0°$) are achieved simultaneously as the HFSS simulation models confirm.

Both 3-element and 9-element HDAAs have been considered as proof-of-concept designs. The choice of the number of elements to be used in an array depends mainly on the specifications associated with its intended applications as well as its fabrication and implementation costs. The choice to develop the 3-element HDAA was simple – it is a cost effective, low complexity, easy to fabricate and measure proof-of-concept pathfinder. It clearly demonstrates the emphasized performance characteristics, i.e., beam steering and broad and stable gain coverage, when the array elements are HDAs. It employs a 3 × 3 version of a low-cost microstrip Butler matrix (BM) feed network which can be scaled to an array of many more elements. It demonstrates that both the HDAA and BM feed network can be realized on a single, ultrathin PCB substrate. It also confirms the analytical and simulation results. Larger HDAAs, e.g., a 9-element array, realize higher maximum gain and narrower beams as the theory and simulations show. These are desired properties for long distance applications such as wireless powered sensor networks. Nevertheless, the realization of its feed network would have been substantially more complicated and expensive, and the resulting HDAA system would not have provided any additional noteworthy fundamental information.

The spacing between the elements was selected to be $D_{space} = 0.45\ \lambda_0$. This choice represents a tradeoff between the size of the array and the resulting peak directivity and FTBR values. As shown in Fig. 10, the simulated peak directivity values are 12.5, 13.9 and 14.5 dBi, and the FTBR values are 8.8, 18.2 and 33 dB, respectively, when the element spacing is 0.35 λ_0, 0.45 λ_0, and 0.55 λ_0. Both the peak

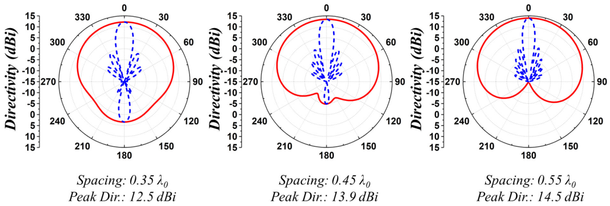

FIGURE 10. Simulated directivity patterns of 9-element HDAAs with different element spacing fed by ideal differential sources at 2.45 GHz.

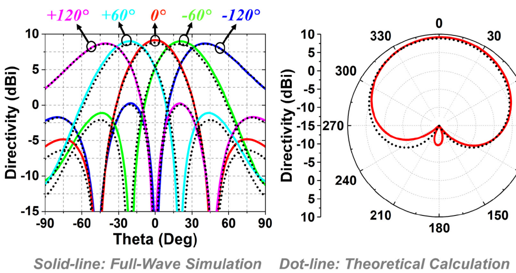

(a)

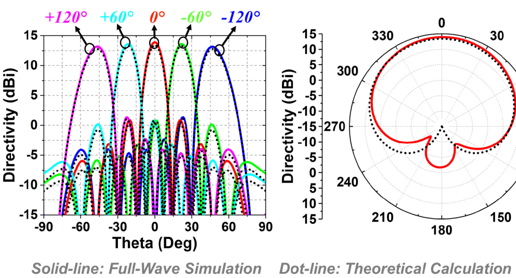

(b)

FIGURE 11. Beam-steering performance comparison of the simulated and theoretical HDAA results. E-plane (left) and H-plane (right) directivity patterns with 0°, ±60° and ±120° phase progression of the elements. (a) 3-element HDAA. (b) 9-element HDAA.

gain and FTBR values decrease if the element spacing is too small. Moreover, well-formed Huygens directivity patterns are obtained once it exceeds 0.45 λ_0. While the directivity and FTBR values reach their peak values if the spacing is 0.55 λ_0, the 0.45 λ_0 spacing was selected for our prototype because a more compact array is realized without sacrificing much performance.

A comparison of their simulated beam-steering performance with the corresponding theoretical HDAAs formed with the ideal HDA element are shown in Figs. 11(a) and 11(b), respectively. Very good correspondence between the performance of the practical and ideal systems is demonstrated. The left subplots present the E-plane directivity patterns when their ports are excited by the same amplitude and with five phase progressions along the array (y-axis), i.e., $-120°$, $-60°$, $0°$, $+60°$ and $+120°$. The E-plane patterns clearly demonstrate the desired beam-steering performance. The beams are symmetrical and the peak directivity variation is very small, i.e., the peak values of the beams in Fig. 11(a) for the five phase progressions are 8.7, 9.0, 9.2, 9.0 and 8.7 dBi, a maximum spread of 0.5 dBi. Note that this small gain variation is in accord with the theoretical results displayed in Fig. 5. The demonstrated scan angles completely cover 130° from $-65°$ to $+65°$. The right subplots present the H-plane patterns when the beam is pointing towards the broadside direction, i.e., along the +z-axis towards ($\theta = 0°$, $\phi = 0°$). The HPBW in the H-plane is wide: 126° from $-58°$ to $+68°$. A large front-to-back-ratio (FTBR) value, 19.0 dB, is attained.

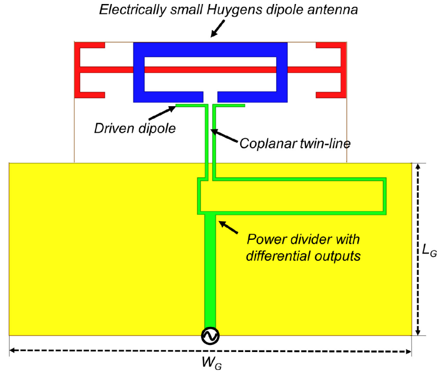

FIGURE 12. Configuration of the HDA excited by a coplanar twin-line integrated with a 50-Ω power divider with differential outputs.

The expected higher directivity of the beams radiated by the 9-element HDAA is clearly seen in Fig. 11(b). The beam-steering performance in the E-plane again shows peak directivity variations that are small, < 0.7 dBi, with values ranging between 13.2 and 13.9 dBi The resulting beam directions for the 5 phase progressions are $-47°$, $-22°$, $0°$, $+22°$ and $+47°$, respectively. All of the first sidelobe levels are less than -11.9 dB. While the beams in the E-plane are narrow, the beamwidth in the H-plane is still very wide and covers 117° from $-59°$ to $+68°$. The FTBR is 18.2 dB, slightly lower than the 3-element array due to the increased mutual coupling that occurs with the larger number of elements in the array.

IV. CO-PLANAR DIFFERENTIAL POWER-DIVIDER IMPLEMENTATION OF THE HDA AND SUBSEQUENT LINEAR HDAAS

The practical realization of the single HDA excited by a microstrip power divider with differential outputs is shown in Fig. 12. The HDA remains the same as in the previous designs. Instead of an ideal source, the short driven dipole is now connected to a coplanar microstrip feedline integrated with a power divider having differential outputs. As illustrated, the power divider yields equal amplitudes, but a 180° phase difference. The simulated $|S_{11}|$ and realized gain values as functions of the source frequency are presented in Fig. 13(a). The HDA remains resonant at the target frequency, 2.45 GHz, and the -10-dB impedance bandwidth now covers 78 MHz from 2.417 to 2.495 GHz, a 3.18% FBW, which is quite satisfactory for the intended narrowband WPT applications. The peak realized gain value is 5.0 dBi and the FTBR reaches 19.8 dB.

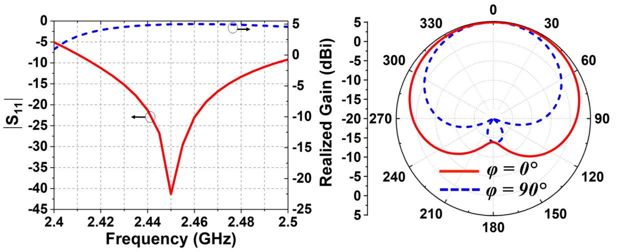

FIGURE 13. Simulated performance of the HDAA whose elements are excited by the co-planar twin-line feed structure with differential outputs. (a) $|S_{11}|$ and realized gain values as a function of the source frequency. (b) Realized gain patterns at 2.45 GHz in the two vertical planes.

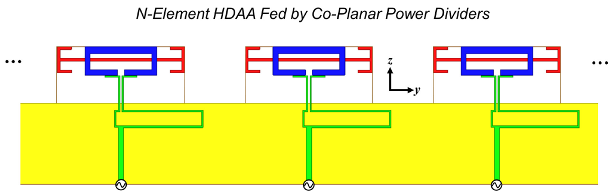

FIGURE 14. Configuration of the linear HDAA whose elements are excited by the co-planar twin-line feed structure with differential outputs.

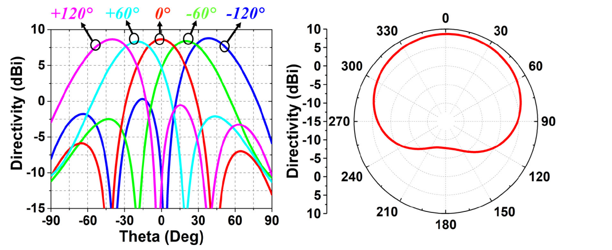

(a)

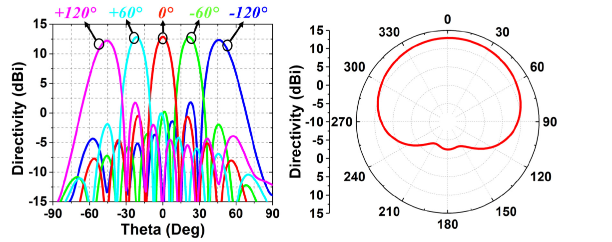

(b)

FIGURE 15. Beam-steering performance of the HDAA whose elements are excited by the co-planar twin-line feed structure with differential outputs. E-plane (left) and H-plane (right) directivity patterns when the elements are excited with equal amplitudes and with the −120°, −60°, 0°, +60° and +120° phase progressions. (a) 3-element. (b) 9-element.

Fig. 13(b) shows the realized gain patterns in the two vertical planes. The patterns are now very symmetric in both vertical principal planes. The HPBW of the H-plane pattern covers 166° from −80° to +86°. Because of the presence of the larger ground plane necessitated by the power divider circuit, the realized gain patterns in the two vertical planes remain cardioid in shape with the same peak and FTBR values, but their shapes are no longer identical. Those peak values change only by 0.8 dB over the entire impedance bandwidth. The realized gain values in the entire upper hemisphere of the H-plane pattern are larger than 1.0 dBi, yielding a gain variation of only 4.1 dB over its 180° span.

A. HDAA DESIGN AND ITS BEAM-STEERING PERFORMANCE

Both the 3-element and 9-element HDAAs excited by the power divider with differential outputs were simulated. The HDAA configuration is shown in Fig. 14. The spacing between the adjacent two elements is again set to $D_{space} = 0.45\ \lambda_0$.

The simulated beam performance of the linear 3-element HDAA is shown in Fig. 15(a). The left subplot presents the E-plane realized gain patterns with the HDAA elements excited with the same amplitude and the −120°, −60°, 0°, +60° and +120° phase progressions. The steered-beams are symmetrical with respect to the broadside direction. Moreover, the peak realized gain varies only 0.4 dBi from 8.4 to 8.8 dBi. The right subplot presents the corresponding the H-plane realized gain pattern for the broadside radiated beam. The beam scan in the E-plane continuously covers 124° from −63° to +61°. The HPBW of the H-plane pattern is very broad, covering 165° from −78° to +87°. The FTBR is 16.4 dB.

The beam-steering performance of the 9-element array is presented in Fig. 15(b). The steered-beams are completely symmetrical with respect to the broadside direction. The peak realized gain variation is only 0.4 dBi from 12.5 to 12.9 dBi when their ports are excited with the same amplitude and with the −120°, −60°, 0°, +60° and +120° phase progressions. The beam pointing angles are −47°, −22°, 0°, +22° and +47°, respectively. All of the sidelobe levels are lower than −10.5 dB. A wide HPBW is observed in the H-plane pattern which covers 157° from −74° to +83°. The FTBR is 15.4 dB. The FTBR is 15.4 dB, slightly lower than the 3-element array due to the increased mutual coupling effects between the larger number of elements in the array.

Fig. 16 presents the simulated active VSWR and mutual coupling performance of the 9-element HDAA as functions of the source frequency. Ports #1 to #9 are assigned from the left to the right of the array. The active VSWR values [39], [40] are obtained when all of the elements are excited with equal amplitudes and with the −120°, −60°, 0°, +60° and +120° phase progressions. These results are shown in Figs. Fig. 16(a)−(e). It is observed that the VSWR values for all nine ports change within a limited range when the scanning angle varies. They are symmetrical with respect to the broadside direction. The overlapped bandwidth for the active VSWR < 2.5 is 600 MHz from 2.425 to 2.485 GHz. Note that this range is sufficient for our targeted WPT applications which do not require wide bandwidths. Moreover, the mutual coupling values $|S_{ij}|$ between the adjacent ports of the array, i.e., $i = j+1$, in the broadside beam case are shown in Fig. 16(f) when port j was driven and all of the other ports were matched to 50 Ω. All of the mutual coupling values are small, less than −12.5 dB from 2.425 to 2.485 GHz.

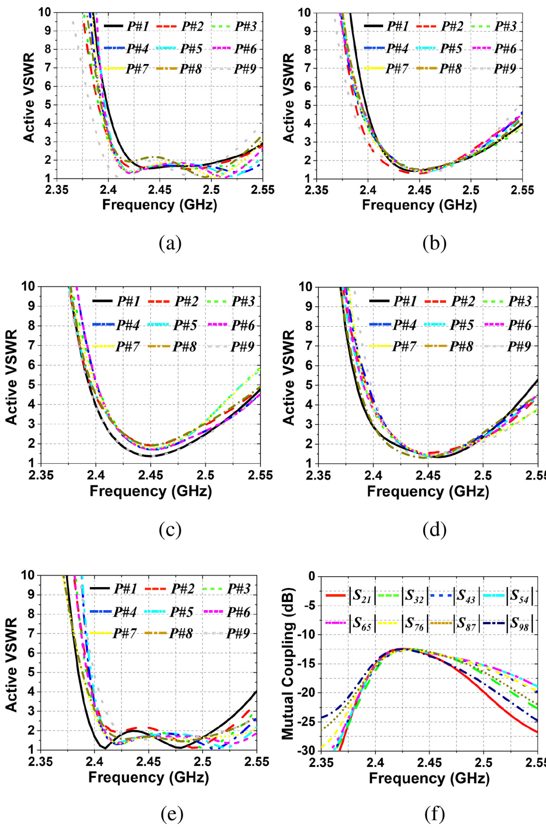

FIGURE 16. Active VSWR of the 9-element HDAA as functions of the source frequency when the elements are excited with equal amplitudes and with the (a) −120°, (b) −60°, (c) 0°, (d) +60° and (e) +120° phase progressions. (f) Associated mutual coupling levels between adjacent ports.

With these excellent beam performance characteristics in the E- and H-planes, the HDAA excited by the power divider with differential outputs is an ideal candidate for wireless applications requiring one point to multi-point high directivity transmissions in one principal vertical plane and broad radiation coverage in the vertical orthogonal one.

B. IMPLEMENTATION AND MEASUREMENT OF THE 3 × 3 BUTLER MATRIX-FED LINEAR 3-ELEMENT HDAA

A proof-of-concept prototype of the 3-element HDAA excited by the by the co-planar twin-line feed structure with differential outputs was realized with a 3 × 3 Butler matrix (BM) implementation. It was fabricated and tested. The entire antenna array configuration is shown in Fig. 17. The air gaps between each HDA element proved to be a very effective decoupling approach. The 3 × 3 BM consists of three 3 dB couplers realized with microstrip lines. When each port, Port#1 to Port#3, of the Butler matrix is excited, the three output ports, Port#4 to Port#6, have the same amplitude, but with a specific phase progression. They are connected to the three HDA elements. Detailed design guidelines of the BM can be found in [23].

Fig. 18 presents the simulated results of the BM alone. All of its outputs have very close amplitudes at and near the targeted 2.45 GHz frequency. Their transmission level is about −4.8 dB when each port is excited. However, they have distinct phase progressions. In particular, all of the output ports have the same phase when Port#1 is excited. The phase progression is −120° (delayed response from Port#4 to Port#6) when Port#2 is excited. The phase progression is +120° (advanced response from Port#4 to Port#6) when Port#3 is excited. Both the amplitude and phase difference of the BM are stable across a very wide bandwidth.

The simulated 3D realized gain patterns of the HDAA when each input port is excited separately are shown in Fig. 19. When one port is excited, the other two

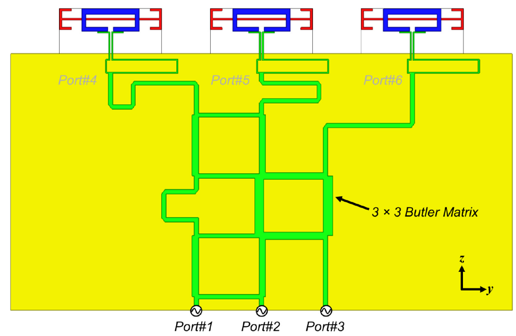

FIGURE 17. Design configuration of the 3 × 3 Butler matrix.

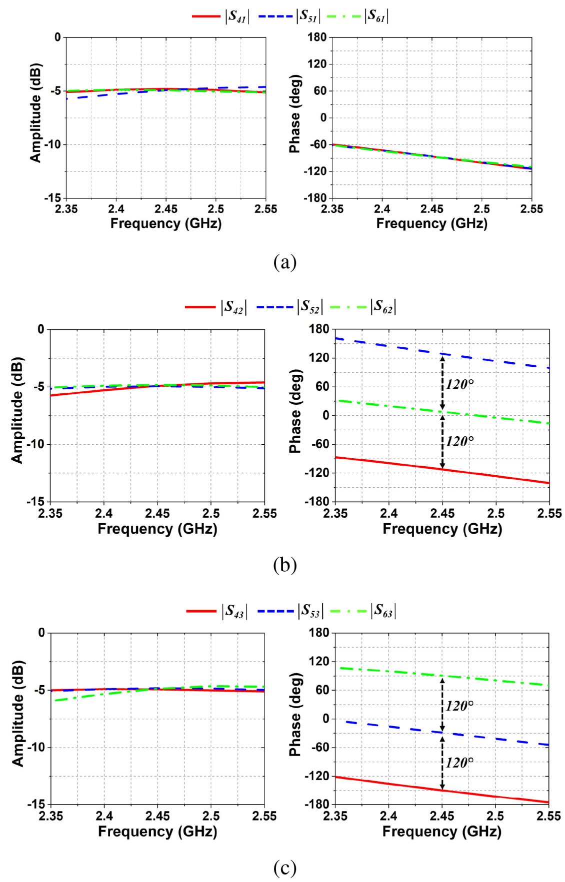

FIGURE 18. Simulated amplitude and phase performance of the S-parameters of the 3 × 3 Butler matrix when each port is excited separately. (a) Port#1. (b) Port#2. (c) Port#3.

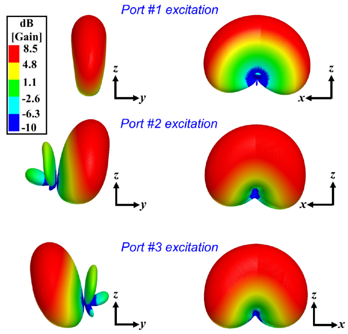

FIGURE 19. Simulated 3D beam-steered radiation patterns of the HDAA when each input port of the BM is excited separately, the other two being terminated in matched loads.

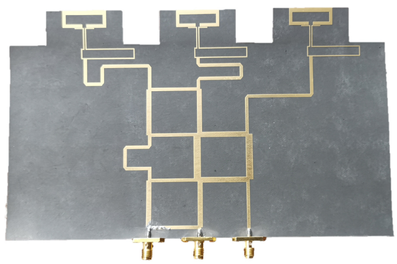

FIGURE 20. Fabricated 3 × 3 Butler matrix-fed 3-element linear HDAA.

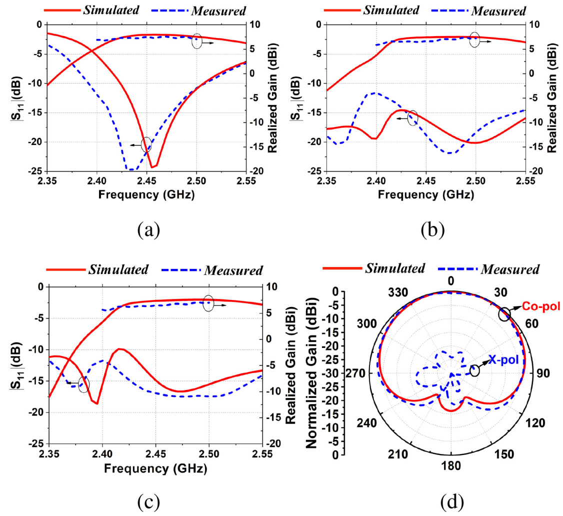

FIGURE 21. Measured and simulated $|S_{11}|$ and realized gain values as a function of the source frequency when (a) Port#1; (b) Port#2; and (c) Port#3 are excited separately. (d) Measured and simulated H-plane normalized realized gain patterns when Port#1 (broadside radiated beam) is excited.

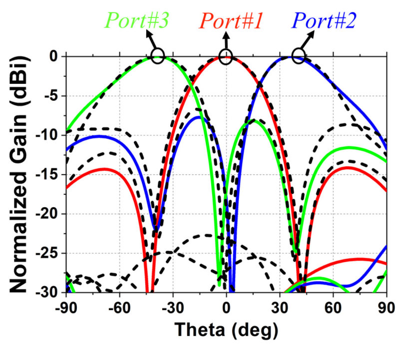

FIGURE 22. Measured (dashed lines) and simulated (solid lines) beam-steered E-plane normalized realized gain patterns of the 3 × 3 BM-fed linear 3-element HDAA prototype when its three ports are excited separately.

are terminated with a 50-Ω load. Good beam-steering performance is realized in the E-plane (left); broad angular coverage is attained. The patterns are very wide in the H-plane (right). Thus, the 3-state system achieves both high directivity and broad angular coverage.

The BM-excited HDAA was fabricated with low-cost PCB manufacturing technology. A photo of it is shown in Fig. 20. Three female SMA connectors were adopted as the signal input ports. The $|S_{11}|$ values were measured with a vector network analyzer (VNA) from Keysight Technologies^{TM}. The radiation patterns were measured in a near-field multi-probe anechoic chamber system.

Figs. 21(a), 21(b), and 21(c) show the measured and simulated $|S_{11}|$ and realized gain values as functions of the source frequency when Port#1, Port#2 and Port#3 are excited, respectively. The measured and simulated results are in reasonably good agreement. The overlapped −10-dB impedance bandwidth covers 110 MHz from 2.395 to 2.505 GHz, a 5.5% FBW. The realized gain values are stable over this impedance bandwidth. Again, this bandwidth is significantly more than sufficient for the intended WPT applications. Moreover, if coverage were desired for short range, low power Wi-Fi communications, e.g., in a WLAN or with a wireless sensor network, or for a higher power, longer range information exchange with, e.g., a drone swarm, it is more than the 100 MHz bandwidth needed to cover the entire 2.4 GHz Industrial, Scientific and Medical (ISM) band. The measured peak realized gain values are 7.6, 7.3, and 7.1 dBi, when Port#1, Port#2 and Port#3 are excited, respectively. Thus, the peak realized gain variation for all three beams was only 0.5 dBi. Fig. 21(d) shows the measured and simulated normalized H-plane realized gain patterns when Port#1 is excited. A very wide HPBW was realized for this broadside radiated beam case that covers 170° from −86° to +84°. A high FTBR, 18.0 dB, was attained.

Fig. 22 shows the measured and simulated normalized radiation patterns when the three ports are individually excited. The measured and simulated results are in very good agreement. The combined E-plane patterns cover a wide angular range. When the beam angle varies over 121° from −63° to +58°, the measured gain variation was only 3.1 dB. Wide-angle coverage in both the E- and H-planes was thus demonstrated.

Table 1 compares the performance characteristics of the developed HDAAs with several other beam-steering linear antenna arrays reported in the literature. In contrast to those systems, our designs employ much smaller elements and, hence, are more dense, yet they achieve relatively better peak realized gains and beamwidths in the vertical plane orthogonal to the array axis. Moreover, our systems exhibit

TABLE 1. Performance comparison of linear antenna arrays with steerable beams.

Ref.	Scale	Center Frequency (GHz)	Total length, Element length (λ_0), (λ_0)	HPBW in the Principal Vertical Plane Orthogonal to the Array	Peak RG	Antenna efficiency	Fabrication process (Antenna type)
[11]	1×4	30.0	4.86, 1.22	$117°$	11.7 dBi	$\sim 80\%$	High-cost metallic (Horn antenna array)
[17]	1×4	37.5	2.62, 0.66	$< 120°$	12.8 dBic	$\sim 50\%$	Single-layer PCB (Slot array)
[24]	1×8	5.5	4.58, 0.57	$\sim 170°$	4.8 dBi	$< 25\%$	High-cost CMOS (Modified dipole array)
[25]	1×8	60.0	5.28, 0.66	$\sim 160°$	12.0 dBi	$\sim 50\%$	Multi-layer PCB (ME dipole array)
Prototype	1×3	2.45	**1.49, 0.30**	**170°**	**7.6 dBi**	**$\sim$ 85%**	**Single-layer PCB (HDAA)**
Simulated	1×3	2.45	**1.49, 0.30**	**164°**	**8.0 dBi**	**$\sim$ 90%**	**Single-layer PCB (HDAA)**
Simulated	1×9	2.45	**4.05, 0.30**	**155°**	**12.5 dBi**	**$\sim$ 95%**	**Single-layer PCB (HDAA)**

the highest antenna efficiencies. These attractive features are highlighted in bold text in the table. Furthermore, the HDA element and, hence, a linear HDAA formed with them is readily scaled to other frequency bands. Consequently, because of the simplicity and ultrathin nature of its design and the high quality board material employed to realize it, analogous versions of our HDAAs at the much higher frequencies of the comparison systems will exhibit essentially the same high efficiencies.

V. CONCLUSION

The theoretical analysis, design simulations and measurements of a set of ultrathin, electrically small Huygens dipole antennas and the uniform linear arrays constructed with those HDA elements were reported. All of the HDAAs exhibited very wide HPBWs in their H-planes and stable gain variation when the beams they radiated were steered in their E-planes. The practical HDAA designs were shown to closely approach those of the ideal systems. A proof-of-concept prototype confirmed the simulated performance characteristics.

With the demonstrated performance characteristics and the attractive practical features such as being ultrathin and realizable with low-cost PCB fabrication, the innovative HDAA systems are ideal candidates for wireless applications that require both short or long distance and multi-user coverage. IoT examples include using them as base station antennas to wirelessly power multiple remotely distributed battery-free elements in a sensor network and to act as the data gateway that collects the data they generate. Moreover, an HDAA in which each HDA is integrated with a rectifier as was achieved in [27] is an ideal candidate as a WPT rectenna array. Because, as noted, our HDA design is readily scaled to many other frequency bands, the associated HDAAs will share the properties described and validated herein. Thus, HDA-based rectenna arrays have the potential to impact many WPT receiver applications associated, for example, with wireless powered IoT systems [41] and with solar power satellite (SPS) and other point-to-point microwave and millimeter-wave power beaming systems [42], [43].

APPENDIX
FAR-FIELDS OF ELECTRIC AND MAGNETIC DIPOLE SOURCES

Because textbooks, e.g., [30], typically only discuss the fields radiated by electric and magnetic currents when their dipole moments are oriented along the z-axis rather than being in an arbitrary direction, we consider that more general case. Recall that the magnetic, $\vec{A}_\omega(\vec{r})$, and electric, $\vec{F}_\omega(\vec{r})$, Lorentz vector potentials in the Lorentz gauge that are associated with the single frequency electric, $\vec{J}_\omega(\vec{r})$, and magnetic, $\vec{K}_\omega(\vec{r})$, current sources are the well-known convolution solutions of the Helmholtz equations they satisfy that relate them directly to those sources, i.e., [30]:

$$\begin{aligned}\vec{A}_\omega(\vec{r}) &= \iiint_V G_\omega(\vec{r},\vec{r}')\left[\mu\vec{J}_\omega(\vec{r}')\right]d^3\vec{r}'\\ \vec{F}_\omega(\vec{r}) &= \iiint_V G_\omega(\vec{r},\vec{r}')\left[\varepsilon\vec{K}_\omega(\vec{r}')\right]d^3\vec{r}'\end{aligned} \tag{21}$$

where V is a volume containing the sources with the source volume element being $d^3\vec{r}'$ and the Green's function of the Helmholtz operator for outgoing waves being

$$G_\omega(\vec{r},\vec{r}') = \frac{e^{-jk|\vec{r}-\vec{r}'|}}{4\pi|\vec{r}-\vec{r}'|} \tag{22}$$

Then, with the textbook far-field approximation for the distance from the source points: $|\vec{r}-\vec{r}'| \sim r - \hat{r}\cdot\vec{r}'$, the far-field vector potential expressions follow immediately:

$$\vec{A}^{ff}_{\omega}(\vec{r}) = \mu \frac{e^{-jkr}}{4\pi r} \iiint_V e^{+jk\hat{r}\cdot\vec{r}'} \vec{J}_{\omega}(\vec{r}') d^3\vec{r}'$$
$$\vec{F}^{ff}_{\omega}(\vec{r}) = \epsilon \frac{e^{-jkr}}{4\pi r} \iiint_V e^{+jk\hat{r}\cdot\vec{r}'} \vec{K}_{\omega}(\vec{r}') d^3\vec{r}' \tag{23}$$

They both have the form of a medium parameter times a spherical wave with respect to the origin of the observation coordinates modified by the three-dimensional Fourier transform of the current densities. Note that these Fourier transforms depend only on the observation angles θ and ϕ since only the unit radial vector is present in them, i.e., $\hat{r} = \vec{r}/r = \sin\theta\, \cos\phi\hat{x} + \sin\theta\, \sin\phi\hat{y} + \cos\theta\hat{z}$.

With the appropriate identities for and manipulations of the grad, curl and div operations required to represent the electric and magnetic fields in terms of those vector potentials and remembering that the associated derivative operations act on the observation coordinates, not the source ones, the far-field expressions of the electric and magnetic fields associated with electric and magnetic current sources are obtained in a straightforward manner:

$$\begin{aligned}\vec{E}^{ff}_{\omega,J} &= -j\omega\left\{\vec{A}^{ff}_{\omega} - \hat{r}\left[\hat{r}\cdot\vec{A}^{ff}_{\omega}\right]\right\}\\ &\equiv +j\omega\hat{r}\times\left[\hat{r}\times\vec{A}^{ff}_{\omega}\right]\\ \vec{H}^{ff}_{\omega,J} &= \frac{1}{\eta}\left(\hat{r}\times\vec{E}^{ff}_{\omega,J}\right)\end{aligned} \tag{24}$$

$$\begin{aligned}\vec{H}^{ff}_{\omega,K} &= +j\omega\hat{r}\times\left[\hat{r}\times\vec{F}^{ff}_{\omega}\right]\\ \vec{E}^{ff}_{\omega,K} &= -\eta\left(\hat{r}\times\vec{H}^{ff}_{\omega,K}\right)\end{aligned} \tag{25}$$

where the wave impedance $\eta = \sqrt{\mu/\varepsilon}$. These results recover the well-known fact that the far fields are transverse electromagnetic (TEM_r) with respect to the unit vector in the observation direction, $\hat{r}$ [30]. If both electric and magnetic current sources are present simultaneously, the total fields are then obtained by superposition, i.e., they simply are the sum of the fields arising from each source separately.

Consider now the idealized electric and magnetic elemental current sources located at the point $\vec{r}_0 = x_0\,\hat{x} + y_0\,\hat{y}$ on the xy-plane:

$$\begin{aligned}\vec{J} &= I_e\ell_e\delta(x-x_0)\,\delta(y-y_0)\,\delta(z)\hat{u}\\ \vec{K} &= I_m\ell_m\delta(x-x_0)\,\delta(y-y_0)\,\delta(z)\hat{v}\end{aligned} \tag{26}$$

where $I_e\ell_e$ and $I_m\ell_m$ represent the electric and magnetic current moments with units $A-m$, i.e., the current density units are A/m^2. The electromagnetic fields in the far field of these xy-plane sources referenced to the coordinate origin follow immediately from (24) and (25):

$$\begin{aligned}\vec{E}^{ff}_{\omega,J} &= -j\omega\mu I_e\ell_e\frac{e^{-jkr}}{4\pi r}e^{+jk\hat{r}\cdot\vec{r}_0}\left\{\hat{u} - \hat{r}\left[\hat{r}\cdot\hat{u}\right]\right\}\\ &= +j\omega\mu I_e\ell_e\frac{e^{-jkr}}{4\pi r}e^{+jk\hat{r}\cdot\vec{r}_0}\left(\hat{r}\times\hat{r}\times\hat{u}\right)\\ \vec{H}^{ff}_{\omega,J} &= \frac{1}{\eta}\left(\hat{r}\times\vec{E}^{ff}_{\omega,J}\right)\\ &= +j\omega\varepsilon\left(\frac{I_e\ell_e}{\eta}\right)\frac{e^{-jkr}}{4\pi r}e^{+jk\hat{r}\cdot\vec{r}_0}\left(-\hat{r}\times\hat{u}\right)\end{aligned} \tag{27}$$

$$\begin{aligned}\vec{H}^{ff}_{\omega,K} &= +j\omega\varepsilon I_m\ell_m\frac{e^{-jkr}}{4\pi r}e^{+jk\hat{r}\cdot\vec{r}_0}\left(\hat{r}\times\hat{r}\times\hat{v}\right)\\ \vec{E}^{ff}_{\omega,K} &= +j\omega\mu\left(\frac{I_m\ell_m}{\eta}\right)\frac{e^{-jkr}}{4\pi r}e^{+jk\hat{r}\cdot\vec{r}_0}\left(\hat{r}\times\hat{v}\right)\end{aligned} \tag{28}$$

It is clear from these expressions that both the electric and magnetic current sources radiate fields that are TEM_r in the far field. Moreover, the expressions in (28) are the dual of those in (27).

Consider now an elemental HDA located at the coordinate origin. It is obtained when the elemental electric and magnetic current density amplitudes are taken to be a balanced pair, i.e., with $I_e\ell_e = I_0\ell$ and $I_m\ell_m = \eta I_0\ell$. Moreover, let their vector directions be specified to match the Huygens dipole antenna configuration in the numerical model, i.e., let $\hat{u} = \hat{y}$ and $\hat{v} = -\hat{x}$. This choice, of course, emphasizes the z-axis as the preferred broadside direction, i.e., $\hat{u}\times\hat{v} = +\hat{z}$. The electric fields, Eq. (1), follow immediately, i.e.,

$$\begin{aligned}\vec{E}^{ff}_{\omega,J}(\vec{r}) &= j\omega\mu\, I_0\ell\frac{e^{-jkr}}{4\pi r}\left(\hat{r}\times\hat{r}\times\hat{y}\right)\\ \vec{E}^{ff}_{\omega,K}(\vec{r}) &= -j\omega\mu\, I_0\ell\frac{e^{ikr}}{4\pi r}\left(\hat{r}\times\hat{x}\right)\end{aligned} \tag{29}$$

Moreover, with the radial unit vector written in terms of Cartesian coordinates, one has

$$\begin{aligned}\hat{r}\times\hat{x} &= \cos\theta\hat{y} - \sin\theta\sin\phi\hat{z}\\ \hat{r}\times\hat{r}\times\hat{x} &= -\left(\sin^2\theta\sin^2\phi + \cos^2\theta\right)\hat{x}\\ &\quad+\ \sin\theta\sin\phi\cos\phi\hat{y} + \sin\theta\cos\theta\cos\phi\hat{z}\\ \hat{r}\times\hat{y} &= -\cos\theta\hat{x} + \sin\theta\cos\phi\hat{z}\\ \hat{r}\times\hat{r}\times\hat{y} &= \sin^2\theta\sin\phi\cos\phi\hat{x}\\ &\quad-\ \left(\sin^2\theta\cos^2\phi + \cos^2\theta\right)\hat{y} + \sin\theta\cos\theta\sin\phi\hat{z}\end{aligned}$$

The explicit expression of the vector pattern of the far-fields, Eq. (3), follows straightforwardly.

ACKNOWLEDGMENT

The authors would like to thank Prof. Lei Ge, Prof. G. L. Huang, and Dr. Shuai Gao, Shenzhen University, for their assistance in the antenna measurements; and Prof. Y. Jay Guo, University of Technology Sydney, for his support of these efforts.

REFERENCES

[1] W. Hong *et al.*, "Multibeam antenna technologies for 5G wireless communications," *IEEE Trans. Antennas Propag.*, vol. 65, no. 12, pp. 6231–6249, Dec. 2017.

[2] R. A. Alhalabi and G. M. Rebeiz, "High-efficiency angled-dipole antennas for millimeter-wave phased array applications," *IEEE Trans. Antennas Propag.*, vol. 56, no. 10, pp. 3136–3142, Oct. 2008.

[3] J. Wang, Y. Li, L. Ge, J. Wang, and K.-M. Luk, "A 60 GHz horizontally polarized magnetoelectric dipole antenna array with 2-D multibeam endfire radiation," *IEEE Trans. Antennas Propag.*, vol. 65, no. 11, pp. 5837–5845, Nov. 2017.

[4] W. Lin and R. W. Ziolkowski, "Wirelessly powered light and temperature sensors facilitated by electrically small omnidirectional and Huygens dipole antennas," *Sensors*, vol. 19, no. 9, p. 1998, Apr. 2019.

[5] J. Zeng and K.-M. Luk, "Wideband millimeter-wave end-fire magnetoelectric dipole antenna with microstrip-line feed," *IEEE Trans. Antennas Propag.*, vol. 68, no. 4, pp. 2658–2665, Apr. 2020.

[6] R. Li, T. Wu, B. Pan, K. Lim, J. Laskar, and M. M. Tentzeris, "Equivalent-circuit analysis of a broadband printed dipole with adjusted integrated balun and an array for base station applications," *IEEE Trans. Antennas Propag.*, vol. 57, no. 7, pp. 2180–2184, Jul. 2009.

[7] N. Nikolic and A. R. Weily, "Compact E-band planar quasi-Yagi antenna with folded dipole driver," *IET Microw. Antennas Propag.*, vol. 4, no. 11, pp. 1728–1734, Nov. 2010.

[8] S. X. Ta and I. Park, "Two-element folded-dipole-driven quasi-Yagi array with low mutual coupling," in *Proc. Int. Workshop Antenna Technol. (iWAT)*, Karlsruhe, Germany, Mar. 2013, pp. 236–239.

[9] L. Lu, K. Ma, F. Meng, and K. S. Yeo, "Design of a 60-GHz quasi-Yagi antenna with novel ladder-like directors for gain and bandwidth enhancements," *IEEE Antennas Wireless Propag. Lett.*, vol. 15, pp. 682–685, 2016.

[10] S. Zhu, H. Liu, Z. Chen, and P. Wen, "A compact gain-enhanced Vivaldi antenna array with suppressed mutual coupling for 5G mmWave application," *IEEE Antennas Wireless Propag. Lett.*, vol. 17, pp. 776–779, 2018.

[11] N. Ashraf, A.-R. Sebak, and A. A. Kishk, "PMC packaged single-substrate 4 × 4 Butler matrix and double-ridge gap waveguide horn antenna array for multibeam applications," *IEEE Trans. Microw. Theory Techn.*, vol. 69, no. 1, pp. 248–261, Jan. 2021, doi: 10.1109/TMTT.2020.3022092.

[12] Q. Sun, Y.-L. Ban, J.-W. Lian, Y. Liu, and Z. Nie, "Millimeter-wave multibeam antenna based on folded C-type SIW," *IEEE Trans. Antennas Propag.*, vol. 68, no. 5, pp. 3465–3476, May 2020.

[13] P. Chen *et al.*, "A multibeam antenna based on substrate integrated waveguide technology for MIMO wireless communications," *IEEE Trans. Antennas Propag.*, vol. 57, no. 6, pp. 1813–1821, Jun. 2009.

[14] L.-H. Zhong, Y.-L. Ban, J.-W. Lian, Q.-L. Yang, J. Guo, and Z.-F. Yu, "Miniaturized SIW multibeam antenna array fed by dual-layer 8×8 Butler matrix," *IEEE Antennas Wireless Propag. Lett.*, vol. 16, pp. 3018–3021, 2017.

[15] J.-W. Lian, Y.-L. Ban, C. Xiao, and Z.-F. Yu, "Compact substrate-integrated 4 × 8 Butler matrix with sidelobe suppression for millimeter-wave multibeam application," *IEEE Antennas Wireless Propag. Lett.*, vol. 17, pp. 928–932, 2018.

[16] Y. Hu, J. Zhan, Z. H. Jiang, C. Yu, and W. Hong, "An orthogonal hybrid analog—Digital multibeam antenna array for millimeter-wave massive MIMO systems," *IEEE Trans. Antennas Propag.*, vol. 69, no. 3, pp. 1393–1403, Mar. 2021, doi: 10.1109/TAP.2020.3016400.

[17] Q. Wu, J. Hirokawa, J. Yin, C. Yu, H. Wang, and W. Hong, "Millimeter-wave multibeam endfire dual-circularly polarized antenna array for 5G wireless applications," *IEEE Trans. Antennas Propag.*, vol. 66, no. 9, pp. 4930–4935, Sep. 2018.

[18] K.-R. Xiang, F.-C. Chen, Q.-X. Chu, and M. J. Lancaster, "A broadband 3 × 4 Butler matrix and its application in multibeam antenna arrays," *IEEE Trans. Antennas Propag.*, vol. 67, no. 12, pp. 7622–7627, Dec. 2019.

[19] Y. Cao, K.-S. Chin, W. Che, W. Yang, and E. S. Li, "A compact 38 GHz multibeam antenna array with multifolded Butler matrix for 5G applications," *IEEE Antennas Wireless Propag. Lett.*, vol. 16, pp. 2996–2999, 2017.

[20] C. Liu, S. Xiao, Y.-X. Guo, M.-C. Tang, Y.-Y. Bai, and B.-Z. Wang, "Circularly polarized beam-steering antenna array with Butler matrix network," *IEEE Antennas Wireless Propag. Lett.*, vol. 10, pp. 1278–1281, 2011.

[21] Y. Zhang and Y. Li, "A dimension-reduction multibeam antenna scheme with dual integrated Butler matrix networks for low-complex massive MIMO systems," *IEEE Antennas Wireless Propag. Lett.*, vol. 19, pp. 1938–1942, 2020.

[22] F. Y. Xia, Y. J. Cheng, Y. F. Wu, and Y. Fan, "V-band wideband circularly polarized endfire multibeam antenna with wide beam coverage," *IEEE Antennas Wireless Propag. Lett.*, vol. 18, pp. 1616–1620, 2019.

[23] M. Ansari, H. Zhu, N. Shariati, and Y. J. Guo, "Compact planar beamforming array with endfire radiating elements for 5G applications," *IEEE Trans. Antennas Propag.*, vol. 67, no. 11, pp. 6859–6869, Nov. 2019.

[24] B. Cetinoneri, Y. A. Atesal, and G. M. Rebeiz, "An 8 × 8 Butler matrix in 0.13-μm CMOS for 5–6-GHz multibeam applications," *IEEE Trans. Microw. Theory Techn.*, vol. 59, no. 2, pp. 295–301, Feb. 2011.

[25] Y. Li and K.-M. Luk, "A multibeam end-fire magnetoelectric dipole antenna array for millimeter-wave applications," *IEEE Trans. Antennas Propag.*, vol. 64, no. 7, pp. 2894–2904, Jul. 2016.

[26] W. Lin, R. W. Ziolkowski, and J. Huang, "Electrically small, low-profile, highly efficient, Huygens dipole rectennas for wirelessly powering Internet-of-Things devices," *IEEE Trans. Antennas Propag.*, vol. 67, no. 6, pp. 3670–3679, Jun. 2019.

[27] W. Lin and R. W. Ziolkowski, "Electrically small, single-substrate Huygens dipole rectenna for ultracompact wireless power transfer applications," *IEEE Trans. Antennas Propag.*, vol. 69, no. 2, pp. 1130–1134, Feb. 2021.

[28] R. F. Harrington, "On the gain and beamwidth of directional antennas," *IRE Trans. Antennas Propag.*, vol. 6, no. 3, pp. 219–225, Jul. 1958.

[29] R. F. Harrington, "Effect of antenna size on gain, bandwidth, and efficiency," *J. Res. Nat. Bureau Stand*, vol. 64, no. 1, pp. 1–12, Jan./Feb. 1960.

[30] C. A. Balanis, *Antenna Theory: Analysis and Design*. Hoboken, NJ, USA: Wiley, 2016.

[31] R. W. Ziolkowski, "Low profile, broadside radiating, electrically small Huygens source antennas," *IEEE Acccess*, vol. 3, pp. 2644–2651, 2015.

[32] M.-C. Tang, H. Wang, and R. W. Ziolkowski, "Design and testing of simple, electrically small, low-profile, Huygens source antennas with broadside radiation performance," *IEEE Trans. Antennas Propag.*, vol. 64, no. 11, pp. 4607–4617, Nov. 2016.

[33] W. Lin and R. W. Ziolkowski, "Electrically small, low-profile, Huygens circularly polarized antenna," *IEEE Trans. Antennas Propag.*, vol. 66, no. 2, pp. 636–643, Feb. 2018.

[34] K.-M. Luk and H. Wong, "A new wideband unidirectional antenna element," *Int. J. Microw. Opt. Technol.*, vol. 1, no. 1, pp. 35–44, Jun. 2006.

[35] L. Ge and K. M. Luk, "A low-profile magneto-electric dipole antenna," *IEEE Trans. Antennas Propag.*, vol. 60, no. 4, pp. 1684–1689, Apr. 2012.

[36] Y. Li, J. Wang, and K.-M. Luk, "Millimeter-wave multibeam aperture-coupled magnetoelectric dipole array with planar substrate integrated beamforming network for 5G applications," *IEEE Trans. Antennas Propag.*, vol. 65, no. 12, pp. 6422–6431, Dec. 2017.

[37] K.-M. Luk and B. Wu, "The magnetoelectric dipole—A wideband antenna for base stations in mobile communications," *Proc. IEEE*, vol. 100, no. 7, pp. 2297–2307, Jul. 2012.

[38] J. Wang *et al.*, "A low-profile vertically polarized magneto-electric monopole antenna with a 60% bandwidth for millimeter-wave applications," *IEEE Trans. Antennas Propag.*, vol. 69, no. 1, pp. 3–13, Jan. 2021.

[39] D. M. Pozar, "The active element pattern," *IEEE Trans. Antennas Propag.*, vol. 42, no. 8, pp. 1176–1178, Aug. 1994.

[40] A. O. Bah, P.-Y. Qin, R. W. Ziolkowski, Y. J. Guo, and T. S. Bird, "A wideband low-profile tightly coupled antenna array with a very high figure of merit," *IEEE Trans. Antennas Propag.*, vol. 67, no. 4, pp. 2332–2343, Apr. 2019.

[41] N. Shinohara, "Trends in wireless power transfer: WPT technology for energy harvesting, mllimeter-wave/THz rectennas, MIMO-WPT, and advances in near-field WPT applications," *IEEE Microw. Mag.*, vol. 22, no. 1, pp. 46–59, Jan. 2021.

[42] N. Shinohara, "History and innovation of wireless power transfer via microwaves," *IEEE J. Microw.*, vol. 1, no. 1, pp. 218–228, Jan. 2021.

[43] C. T. Rodenbeck *et al.*, "Microwave and millimeter wave power beaming," *IEEE J. Microw.*, vol. 1, no. 1, pp. 229–259, Jan. 2021.

WEI LIN (Senior Member, IEEE) received the bachelor's and master's degrees in electronic engineering from the South China University of Technology, Guangzhou, China, in 2009 and 2012, respectively, and the Ph.D. degree in electronic engineering from the City University of Hong Kong, Hong Kong, in 2016.

He is currently a Lecturer with the University of Technology Sydney, Ultimo, NSW, Australia. He worked as a Research Associate with Nanyang Technological University, Singapore, from August 2012 to August 2013, as a Postdoctoral Research Associate and then a Chancellor's Postdoctoral Research Fellow, from October 2016 to May 2021 with the Global Big Data Technologies Centre, School of Electrical and Data Engineering, Faculty of Engineering and IT, UTS. His research interests include the designs of circularly polarized antennas, electrically small antennas, reconfigurable antennas, HF antennas, satellite antennas, millimeter-wave antennas, wireless power transfer, terahertz devices, and their applications.

Dr. Lin has received many academic awards, which mainly include the Australia Research Council Discovery Early Career Researcher Award in 2021, the 2019 Raj Mittra Travel Grant (RMTG2019) from the IEEE AP-Society, the Best Paper Award (First Prize) at the International Symposium on Antennas and Propagation in 2018, the Best Young Professional Paper Award (First Prize) at the 3rd Australian Microwave Symposium in 2018, the Best Poster Paper Award at the 2nd International Conference on Electromagnetic Materials and Technologies for the Future in 2017, a Talent Development Scholarship from the Hong Kong Government, and the Young Scientist Award at the IEEE Region 10 Conference in 2015. He was a recipient of an Outstanding Reviewer Award from the IEEE ANTENNAS AND WIRELESS PROPAGATION LETTERS in 2018, and the IEEE TRANSACTIONS ON ANTENNAS AND PROPAGATION in 2020.

RICHARD W. ZIOLKOWSKI (Life Fellow, IEEE) received the B.Sc. (*magna cum laude*) degree (Hons.) in physics from Brown University, Providence, RI, USA, in 1974, the M.S. and Ph.D. degrees in physics from the University of Illinois at Urbana–Champaign, Urbana, IL, USA, in 1975 and 1980, respectively, and an Honorary Doctorate degree from the Technical University of Denmark, Kongens Lyngby, Denmark, in 2012.

He is currently a Distinguished Professor with the Global Big Data Technologies Centre, Faculty of Engineering and Information Technologies, University of Technology Sydney, Ultimo, NSW, Australia. He became a Professor Emeritus with the University of Arizona in 2018, where he was a Litton Industries John M. Leonis Distinguished Professor with the Department of Electrical and Computer Engineering, College of Engineering and was also a Professor with the College of Optical Sciences. He was the Computational Electronics and Electromagnetics Thrust Area Leader with the Engineering Research Division of the Lawrence Livermore National Laboratory, before joining The University of Arizona, Tucson, AZ, USA, in 1990. His current research interests include the application of new mathematical and numerical methods to linear and nonlinear problems dealing with the interaction of electromagnetic and acoustic waves with complex linear and nonlinear media, as well as metamaterials, metamaterial-inspired structures, nano-structures, and other classical and quantum applications-specific configurations.

Prof. Ziolkowski was the recipient of the 2019 IEEE Electromagnetics Award (IEEE Technical Field Award). He was the 2014–2015 Australian DSTO Fulbright Distinguished Chair in Advanced Science and Technology. He served as the President of the IEEE Antennas and Propagation Society (AP-S) in 2005 and has had many other AP-S leadership roles. He is also actively involved with the International Union of Radio Science (URSI), the European Association on Antennas and Propagation, and the International Society for Optics and Photonics (SPIE) professional societies. He became a Fellow of the Optical Society of America in 2006, and the American Physical Society in 2016.